Progress Toward Accurate Measurement of Dielectric Barrier Discharge Plasma Actuator Power

David E. Ashpis
NASA, Cleveland, Ohio 44135

Matthew C. Laun
HX5 Sierra LLC, Cleveland, Ohio 44135

and

Elmer L. Griebeler
Vantage Partners LLC, Cleveland, Ohio 44135

The accurate measurement of power consumption by dielectric barrier discharge plasma actuators is a challenge due to the characteristics of the actuator current signal. Microdischarges generate high-amplitude, high-frequency current spike transients superimposed on a low-amplitude, low-frequency current. A high-speed digital oscilloscope was used to measure the actuator power consumption using the shunt resistor method and the monitor capacitor method. The measurements were performed simultaneously and compared to each other in a time-accurate manner. It was found that low signal-to-noise ratios of the oscilloscopes used, in combination with the high dynamic range of the current spikes, make the shunt resistor method inaccurate. An innovative, nonlinear signal compression circuit was applied to the actuator current signal and yielded excellent agreement between the two methods. The paper describes the issues and challenges associated with performing accurate power measurements. It provides insights into the two methods including new insight into the Lissajous curve of the monitor capacitor method. Extension to a broad range of parameters and further development of the compression hardware will be performed in future work.

Nomenclature

C	=	capacitance
I	=	current
P	=	power
$\overline{P_a}$	=	average power
$\dot{P}(t)$	=	average power evolution at time, t
Q	=	charge
R	=	resistance
T	=	period
t	=	time

Subscripts

a	=	actuator, average
m	=	monitor capacitor

I. Introduction

APPLICATIONS of dielectric barrier discharge (DBD) plasma actuators for aerodynamic flow control became an active research area in the last decade. A DBD actuator is a device that consists of a pair of electrodes separated by a dielectric. One electrode is exposed to the flow, and the other is covered. Alternating current (ac) voltage in the kilovolt range is applied to the electrodes and creates surface discharge plasma on the exposed electrode (Fig. 1).

There are usually two modes of operation. Conventional DBD operation (AC-DBD) involves application of a voltage waveform in the kilohertz frequency range, with or without modulation or pulsing. In this mode, heat generation is insignificant, and the actuator generates momentum in the form of a wall jet parallel to the surface. The wall-jet momentum coupling with the external flow is the foundation for active flow control. The other mode of DBD operation involves applying voltage consisting of ultrashort, repetitive pulses (NS-DBD). The pulses are usually several nanoseconds wide, and the repetition rate ranges from a few hundred hertz to a few hundred

kilohertz. In this mode of operation, the generated momentum is negligible, but there is a fast, localized heating of the gas that creates pressure waves or even shock waves. The repetition generates pressure oscillations that are used for active flow control. For the AC-DBD actuator, see review articles by Moreau [1], Corke et al. [2–4], Benard and Moreau [5], and Kotsonis [6]. For the NS- DBD actuator, see the paper by Roupassov et al. [7]. Combinations of AC-DBD and NS-DBD were also reported by Starikovskiy et al. [8].

This project is limited to the conventional, momentum-generating AC-DBD actuator operation (kilohertz-range applied voltage frequency). The interest is to characterize the aerodynamic and electrical performance of the actuator. Generally, it is performed first without external flow. The aerodynamic properties are determined by measuring the induced wall jet using a pitot tube, hot-wire anemometry, or particle image velocimetry (PIV). They can also be determined by measuring the thrust with a load cell or a force balance. Measurements of the electrical properties include recording the applied voltage and the resulting current for a given waveform and frequency (see for example Thomas et al. [9]). Resulting calculations include actuator power consumption and actuator impedance. The time signature of the instantaneous power evolution may aid in identifying plasma and flow behaviors.

This paper is focused on characterization of the power consumption of the DBD actuator, which is important for several reasons. First, it is an important parameter in comparative characterization of performance of different actuator designs. There are many comparisons of actuator performance reported in the literature. However, in most cases, the comparisons are meaningful only if they are made at constant power. Second, in practical implementations of flow control systems, actuator power consumption data is needed for cost–benefit analysis of the system. Wind-tunnel or flight tests establish the aerodynamic performance benefits, and the power consumption of the actuators is a major portion of the cost or penalty. The third reason is that consumed power data are needed for design of efficient and lightweight high-voltage power supplies.

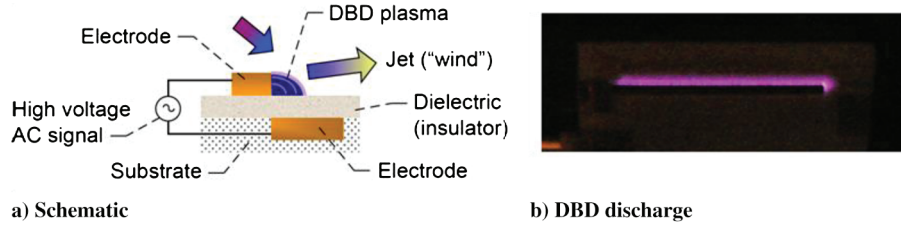**a) Schematic**   **b) DBD discharge**

Fig. 1   DBD plasma actuator: a) schematic of a DBD plasma actuator, and b) top view of a DBD discharge (alumina dielectric actuator experiment at NASA Glenn Research Center).
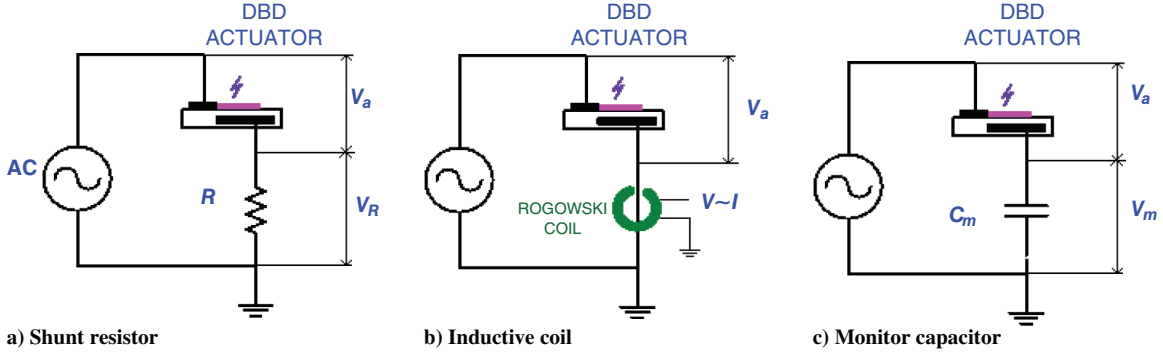

a) Shunt resistor   **b) Inductive coil**   **c) Monitor capacitor**

Fig. 2   Electrical circuit diagrams: a) shunt resistor method, b) inductive current measurement method, and c) monitor capacitor method.

Additional reasons are the proposed uses of real-time power metering for health monitoring of the actuator (Kriegseis et al. [10]) and as a sensor providing input to closed-feedback loop active flow control systems (Kriegseis et al. [11]).

Power measurements of DBD plasma actuators were performed by many researchers. However, as found in a survey reported in Kriegseis et al. [12], there are large discrepancies in the published literature. The power is usually calculated from the measured voltage and current waveforms. In the case of DBD actuators, even though the voltage waveform is generally a smooth signal, the current waveform is not. It is characterized by fast, dynamic spikes, which are more difficult to acquire and resolve with sufficient accuracy. Therefore, power measurement is not as straightforward as it seems and requires closer attention to the measurement technique and the data acquisition instruments.

This paper addresses issues associated with accurate DBD power measurements and reports on the progress we made toward achieving this goal. We performed power measurements using two methods simultaneously. The two methods are compared, and a promising improvement technique is proposed. The measurements were taken with a limited number of parameter ranges and actuator designs. Extending and validating the technique for a broad range of operating parameters and actuators designs is planned for the near future.

A.   Power Consumption Measurements Methods

There are two methods to measure power: 1) electric current method, and 2) electric charge method.

1.   Electric Current Methods

In the current-based methods, a time series of the voltage and current signals are recorded. The instantaneous power is calculated by multiplication of the two signals:

$$P(t) = V(t)I(t) \qquad (1)$$

where $V(t)$ is the voltage on the actuator, $I(t)$ is the actuator current, and $P(t)$ is the instantaneous power.

The averaged power $\overline{P_a}$ is calculated by averaging the instantaneous power over one cycle (period) T:

$$\overline{P_a} = \frac{1}{T} \int_0^T V(t)I(t)\, dt \qquad (2)$$

We will define the averaged power evolution as

$$\bar{P}(t) = \frac{1}{t} \int_0^t V(t')I(t')\, dt' \qquad (3)$$

Hence, the single-cycle-averaged power is equal to the averaged power evolution at the end of the cycle:

$$\overline{P_a} = \bar{P}(t = T) \qquad (4)$$

There are two techniques to measure the current.

a.   Current Measurement Using a Shunt Resistor.   A shunt resistor with known resistance R is placed in series between the covered electrode and ground (Fig. 2a). The current is calculated from the voltage V_R measured across the shunt resistor using Ohm's law. The shunt provides a voltage low enough for measurement by instruments. Typical values of shunt resistors used are in the range of 1–100 Ω for actuator geometries commonly used in published studies. The shunt has relatively low impedance compared to the actuator impedance, which is in the megohm range during most of the ac cycle.

b.   Current Measurement Using an Inductive Coil.   Another method is to measure the current using an inductive Rogowski coil (Fig. 2b). A coil that is often reported to be used by the research community for this purpose is the Pearson Model 2100.‡ Another available coil with a higher upper frequency bandwidth limit is the Pearson Model 6585 (see footnote ‡). We are not aware of the latter being used in published literature. We decided not to use the inductive current measurement method because we concluded that it is not adequate for the source signal. This will be discussed in a later section.

2.   Electric Charge Method

One technique is described for this method.

a.   Charge Measurement Using a Monitor Capacitor.   In this method, an integrating capacitor with a known capacitance is used (usually called a monitor capacitor but also called a measurement or probe capacitor). It is placed in series between the covered actuator electrode and ground (Fig. 2c). The monitor capacitor creates an ac

voltage divider with the actuator impedance, which is mostly capacitive. The monitor capacitor capacitance value C_m is chosen to be large compared to the capacitance of the actuator without plasma discharge (sometimes called "cold" capacitance). Because the capacitance of typical actuators used in published studies is very low (5–200 pF), typical monitor capacitors are selected with a value between 10 and 330 nF. The capacitance is usually selected to provide a voltage that is adequately low for measurement by instruments. Because the monitor capacitor does not have to withstand high voltages, it allows for a greater selection from manufacturers. The capacitance of the monitor capacitor is desired to be constant over the operating voltage and frequency range of the actuator. Careful selection of the capacitor model can provide this condition.

The capacitor-based charge method is described as follows.

The instantaneous charge on the monitor capacitor is

$$Q_m(t) = C_m V_m(t) \tag{5}$$

And the current through the capacitor is

$$I_m(t) = C_m \frac{dV_m(t)}{dt} \tag{6}$$

where Q_m is the charge on the capacitor, V_m is the voltage across the capacitor, C_m is the capacitor capacitance (assumed to be constant), and I_m is the current through the capacitor.

Because the current through the monitor capacitor must be identical to the current through the actuator (because they are in series), $I_m = I_a$, the instantaneous power dissipated by the actuator is

$$P_a(t) = V_a(t) \cdot I_a(t) = V_a(t) \cdot C_m \frac{dV_m(t)}{dt} \tag{7}$$

where V_a is the voltage across the actuator, and I_a is the current through the actuator.

The average power over a period T is obtained using Eq. (7) and change of variables:

$$\bar{P}_a = \frac{1}{T} \int_0^T V_a(t) \cdot C_m \frac{dV_m(t)}{dt}\, dt = \frac{1}{T} \int V_a \cdot C_m\, dV_m$$

$$= \frac{1}{T} \oint_{\substack{\text{one} \\ \text{cycle}}} V_a\, dQ_m \tag{8}$$

The instantaneous capacitor charge Q_m and the instantaneous actuator voltage V_a plotted against each other generate a Lissajous curve in the Q_m–V_a plane. Equation (8) shows that the area inside the closed Lissajous curve divided by the ac cycle period T is equal to the actuator power.

Voltage and current signals as well as power measurements were recorded and reported in reports and publication by numerous researchers. Most of the reported work used the current-based

methods of measuring power either by shunt resistor technique or inductive coil technique. The capacitor-based charge method was less common among the DBD plasma aerodynamic community until recently. The charge method was originally introduced by Manley [13] for discharge between parallel plates. The method is also described in Wagner et al. [14] and Borcia et al. [15] in their work related to material processing with plasma. In context of DBD plasma actuators for aerodynamics, the method was first used by Pons et al. [16]. It was later used by Hoskinson [17] and Poon [18]. Extensive studies and applications of the charge method were recently made by Grundmann and Tropea [19] and Kriegseis et al. [10–12,20].

B. Motivation

Our interest in the power characterization was motivated by observing the spiky current signals and the spiky appearance of the Lissajous curve in the published literature. An example is shown in Fig. 3 taken from Pons et al. [16]. Figure 3a displays large-amplitude current spikes superimposed on a low-amplitude current signal, consistent with observations of others. The spikes are different in the forward stroke (decreasing applied voltage) and the backward stroke (increasing applied voltage) of the actuator operation, as defined and observed by Enloe et al. [21,22]. It is known that the current spikes are associated with microdischarges or streamers that constitute the DBD discharge. Each microdischarge is causing a fast electrical impedance change within the actuator that results in a current spike. The spikes are of ultrashort duration (less than 100 ns) and occur at seemingly random time intervals that are much shorter than the ac cycle period. The current spikes also have extreme dynamic range when comparing the signal's peak to the average value ratio ("crest factor"). This raises the question regarding the data acquisition rate and resolution required to resolve the spikes and their impact on accuracy of the current-based power measurement method.

Observing the Lissajous curves reported in literature also raises questions (Fig. 3b for example). Because the two-dimensional curve is derived from a smooth voltage and the charge from an integrating capacitor, it is expected to be a smooth curve. However, the experimental results show spikes in the direction of the charge axis. It therefore raises questions about the origin of these spikes and their role in the power calculation with the capacitor-based charge method. Our project attempts to provide some answers to these questions.

II. Experimental Setup

A. Approach: Simultaneous Actuator Power Measurements

Our approach was to measure the power consumption using both the monitor capacitor method and the shunt resistor method and then compare the two. Because the distribution of the current spikes made the current signal nonperiodic and pseudorandom, we chose to perform a time-accurate comparison, and therefore we conducted the measurements using both methods simultaneously. We used the circuit shown in Fig. 4. The capacitor and resistor were placed in series between the actuator and the ground. This required measuring the differential voltage across the capacitor because the voltage on the
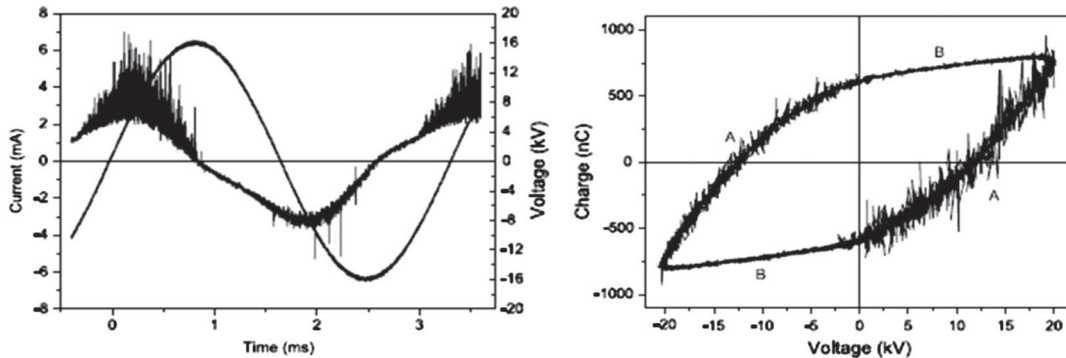

a) Voltage and current

b) Lissajous curve

Fig. 3 Representations of a) applied voltage and current, and b) Lissajous curve (from Pons et al. [16], reprinted with permission).
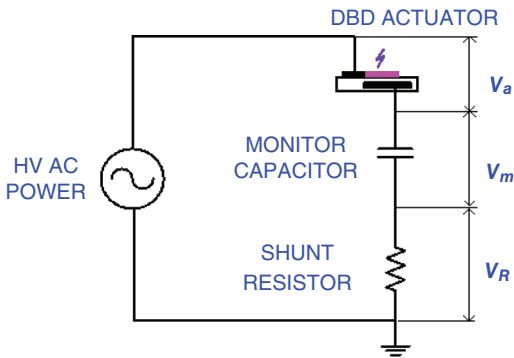
Fig. 4 Circuit for simultaneous monitor capacitor and shunt resistor methods.

Fig. 6 Schematic of the test setup.

shunt resistor is not negligible. If the measurement is performed with only one method, then a single-ended probe would be sufficient.

B. Test Article

The actuator test article is shown in Fig. 5. The electrodes were made of copper tape 0.04 mm (1.4 mil) thick with a conductive adhesive layer of 0.03 mm (1.2 mil). The exposed electrode was 6 mm wide. The grounded electrode was 50 mm wide, which is more than sufficient to not inhibit the longitudinal extension of the plasma. The span of both electrodes was 100 mm. The bottom electrode edge was insulated with tape to prevent discharge. The back edge of the exposed electrode was also insulated with tape to prevent discharge, although no (or insignificant) discharge was expected there. The sides of the exposed electrode were also insulated to prevent edge discharges. There was no offset gap between the exposed and covered electrodes. The dielectric material was Plexiglas acrylic 1.4 mm thick.

C. Instrumentation Setup

Figure 6 shows a schematic of the experimental setup. The power was provided by a Trek Inc. Model 20/20C high-voltage amplifier fed with a Stanford Research Systems signal generator Model DS345. High voltage was usually measured with the voltage monitor built into the Trek amplifier. The current monitor built into the Trek amplifier was found to be too limited in accuracy and was not used. A Tektronix P6015A high-voltage probe was also used in the course of this project.

There was a slight difference in voltage measured between the internal Trek voltage monitor and the external Tektronix high-voltage probe. The Trek monitor could only show the voltage at the local output of the amplifier and not the voltage on the exposed actuator electrode. Voltage differences between the two points existed due to the interconnecting high-voltage cable that has nonzero impedance.
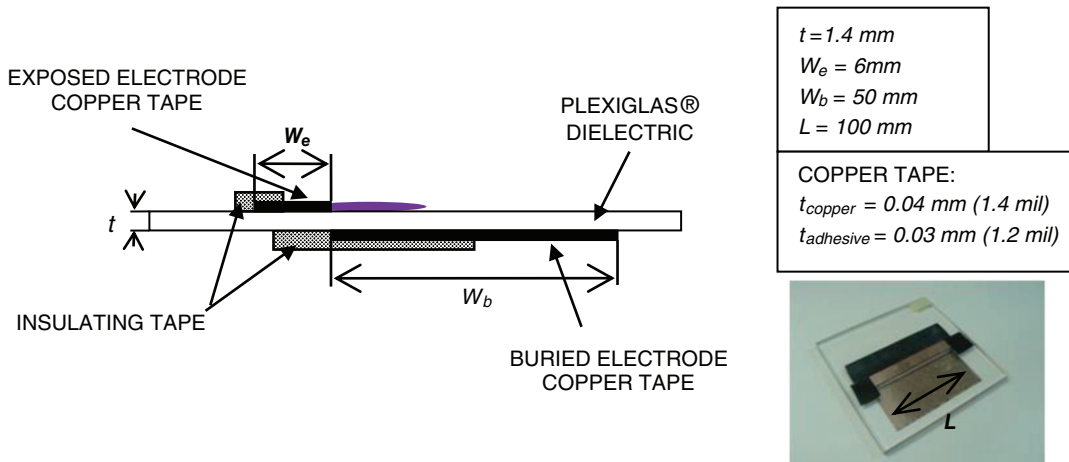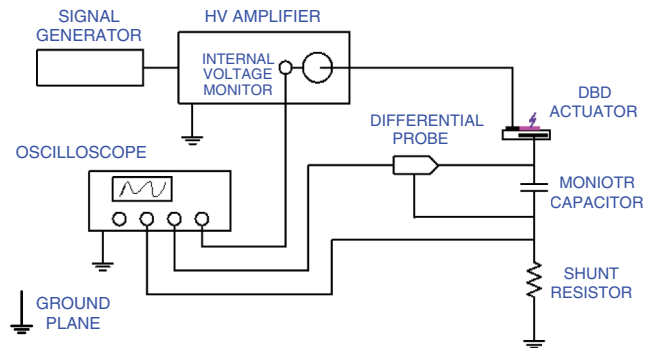
With the Tektronix high-voltage probe, measurement was able to be made directly on the actuator as close as possible to the exposed electrode. The probe was located near the actuator, and the input was connected to the exposed electrode, whereas the ground was connected to the ground plane. However, our experience revealed that the presence of the probe near the actuator affected the actuator behavior and consequently the measured results. This was determined to be due to the parasitic capacitance of the probe being added to the end of the high-voltage power supply cable, which altered the apparent impedance seen by the exposed actuator electrode. Therefore, we chose to use the built-in Trek amplifier voltage monitor and neglect the relatively minor voltage differences caused by the high-voltage cable.

All the voltages were measured with a high-speed oscilloscope LeCroy Model WaveRunner HRO 66Zi. Additional details are given in the next section.

D. Provisions for Improved Measurements

To conduct higher accuracy measurements, several steps were taken to minimize parasitic inductance, parasitic capacitance, conducted interference, radiated interference, and transmission line effects, as follows.

1) Grounding and shielding: A large copper sheet (30 × 46 cm, or 12 × 18 in.) was used as ground plane. The copper sheet was grounded to earth ground at one point only (via a dedicated laboratory ground lead or via the return lead of the Trek amplifier, which is internally connected to the line voltage ground). All the components were placed on the copper sheet. The ground leads of the components or probes were connected to the ground plane. This included the high-voltage amplifier return lead, high-voltage probe ground, monitor circuit ground, etc. A low-capacitance (17 pF) power isolation transformer (Corona Magnetics Inc. Model CMI 6487) was used to isolate the line voltage power connection to the oscilloscope. The isolation between the transformer primary and secondary coils minimized ground-loop interference due to unintended common-mode noise current. That current might flow

Fig. 5 DBD plasma actuator test article: geometry and dimensions.

Fig. 7 Experimental setup, showing actuator test article viewed from the covered electrode side, copper ground plane, flat copper tape leads, and capacitor–resistor assembly with differential probes attached.

Fig. 8 Capacitors and resistors used: a–b) mica capacitors, c) chip capacitor, d) chip resistor, and e) metal film resistor in TO-220 case.

through the oscilloscope and probe leads and potentially corrupt the low-level actuator signals. The high-voltage amplifier power input was connected directly to the lab wall outlet for safety. These measures minimized ground loops, minimized conducted noise, and promoted a single reference ground potential as closely as possible. Protective foil shielding was also connected to the ground plane and applied over sensitive monitor circuits and exposed probe tips to minimize radiated noise from the plasma discharges on the actuator.

2) Minimizing parasitic inductance: Flat, copper conductors were used instead of round conductors to minimize parasitic lead inductance as much as possible. Flat, braided conductors were used to connect the amplifier and oscilloscope grounds separately to the ground plane. An image of the installation is shown in Fig. 7 (the temporary red probes were not used in the final experiment).

3) High-speed data acquisition: Data acquisition was performed using high-speed oscilloscopes in an attempt to resolve the high-frequency spikes. The project started with a Tektronix DPO 7254 (8 bits, 2.5 GHz analog bandwidth, 10 GS/s per channel at four active channels). Later, we switched to a LeCroy WaveRunner HRO 66Zi oscilloscope (12 bits, 600 MHz analog bandwidth, 2 GS/s per channel at four active channels). The data presented in this report were acquired with the latter. The oscilloscopes were operated in the raw "sample" mode (no scope phase averaging, no scope "hi-res" mode, etc.).

4) Differential voltage measurements: A differential probe, LeCroy Model AP034 (1 GHz bandwidth), was used in conjunction with the LeCroy oscilloscope. The advantage over using two single-ended probes is that the actual voltage across the monitor capacitor could be measured directly without introducing the uncertainty and noise from an additional oscilloscope channel and a separate ground reference voltage.

5) Monitor capacitor type: We have chosen low-inductance, equivalent-series-resistance (ESR), low-charge-leakage capacitors for the monitor capacitor. The types and models of capacitors used were:

   a) Dipped silvered mica capacitor (CDE Cornell Dubilier, CD30 or CD42 series): this capacitor has very good properties, but its packaging, mainly the parasitic inductance of the leads, may diminish some of its advantages.

   b) Ceramic chip capacitor (Kemet NP0 2220 series, e.g., P/N C2220C334J1GACTU): this capacitor has the advantage that it has a small size and has no leads because it is intended to be surface-mounted directly on a printed circuit board (PCB). It allowed a compact connection as explained in a later paragraph. This capacitor type was used in the final circuit.
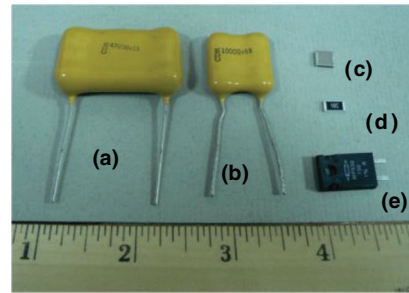
6) Shunt resistor type: The shunt resistor used was a monolithic, metal-film type packaged in either a TO-220 style (Caddock Electronics, Inc., e.g., P/N MP930-100-1%) or a chip resistor package (Panasonic 2512 series, e.g., P/N PT2.0YCT). The latter is PCB surface-mountable allowing compact connection and minimum parasitic lead inductance. It was used in the final circuit. An image of the capacitors and resistors used is shown in Fig. 8.

7) Rogowski coils: We have chosen not to use Rogowski coils to measure current because of their upper and lower bandwidth limits. As indicated previously, the Rogowski coil popular in published literature is the Pearson Model 2100 (frequency range: 125 Hz to 20 MHz at −3 dB). The Pearson Model 6585 has a better high-frequency limit but poorer low-frequency response (frequency range: 400 Hz to 250 MHz at −3 dB). The high-frequency limit is of concern because it is low enough to attenuate and distort the high-frequency current spikes, even with the higher-frequency model.

The low-frequency limit is as important a constraint as the high-frequency limit and is also of concern; as will be shown in a later section, the vertical asymmetry and nonrepetitive, random time distribution of the current spikes create a significant low-frequency component (less than 100 Hz) in the current waveform, which is severely attenuated by these inductive coil frequency ranges. The shunt resistor chip is naturally full bandwidth with nearly no frequency limits in our frequency range of interest.

E. Measurement Issues and Constraints

Several attempts were made in the course of the project to achieve accurate measurements of the power by continuously improving the circuits and the current measurement techniques. Only the final technique and configuration are presented in this paper. The circuit used for the final measurements was constructed by soldering a chip capacitor and a chip resistor to each other in series, as shown in Fig. 9.

1. Oscilloscope Vertical Resolution and Accuracy

Measuring the current signal was a challenge because of its large dynamic range. The current signal has a very large crest factor (ratio of the large-amplitude spikes to the low-amplitude signal). As will be shown in Sec. III, our crest factor was significantly larger than that

Fig. 9 Chip capacitor–chip resistor arrangement.

5

a) Schematic of two-diode compression circuit

c) Compression circuit attached to monitor capacitor and shunt resistor

b) Diode compression circuit transfer function (Purple). Straight line (Red) is linear for reference
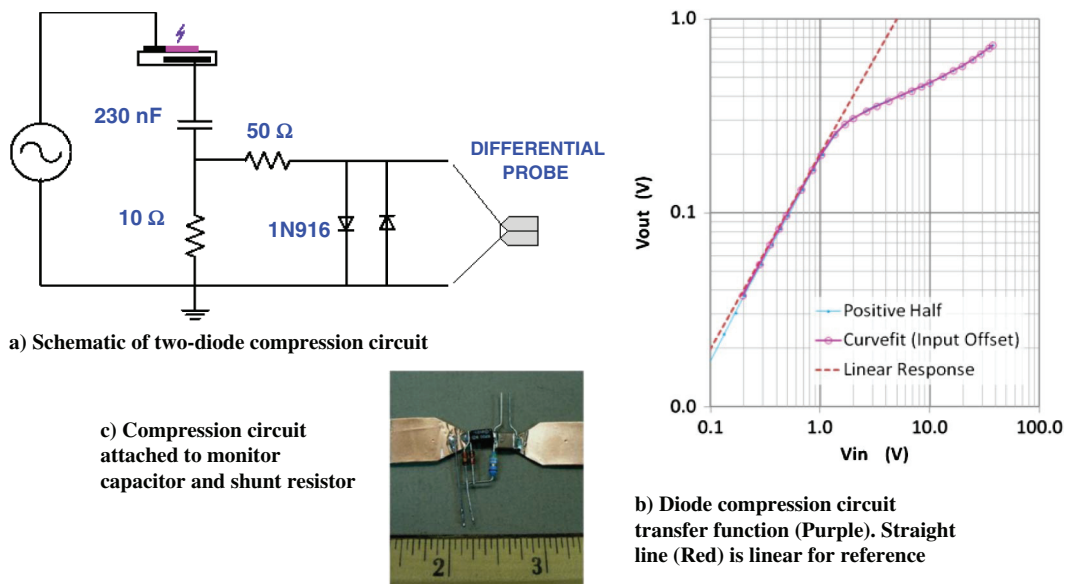
Fig. 10   Nonlinear compression circuit.

shown in the example of Fig. 3a. Because of the crest factor, the Tektronix oscilloscope was not able to simultaneously resolve the high-amplitude current spikes and the low-amplitude background current with adequate certainty. The reasons were the finite 8 bit quantization range, a lower effective resolution represented by its effective number of bits (ENOB) figure, and insufficient signal-to-noise ratio (SNR), which was largely due to the noise floor of the instrument at the required vertical voltage scale setting.

The LeCroy oscilloscope was used next to improve the finite quantization range from 8 to 12 bits (a theoretical improvement of resolution by a factor of 16). It was a compromise because it had a lower analog frequency bandwidth and a lower maximum data acquisition rate as compared to the Tektronix. However, the increased quantization bits allowed improvement of the ENOB figure and the resulting certainty. Also, the LeCroy memory size allowed for storing 64 consecutive, 2 kHz ac cycles acquired at 2 GS/s sampling rate. Even though the increased vertical resolution was a major improvement, we learned that the SNR and the noise floor were still not yet satisfactory to resolve the large spikes and the low-amplitude signal simultaneously.

In summary, the oscilloscope vertical resolution was the major issue encountered in this investigation. Additional details are provided as follows. Although the data acquisition hardware module in an oscilloscope uses a fixed number of bits for quantization, it does not imply that the full analog vertical range has the same resolution. Because the oscilloscope analog input channel hardware includes internal analog amplifiers, there is inherent noise and distortion present. The internal analog-to-digital converter also contributes noise and distortion that varies with the sampling rate. The total of the amplifier noise, quantization noise, and other random error sources constitutes the noise floor. In combination with the finite quantization bit number and analog-to-digital converter effects, it generates an effective number of bits (ENOB), which reduces the nominal resolution of the instrument substantially.

The ENOB depends on many parameters. One of them is the data acquisition rate, and the ENOB generally decreases with increasing sample rate. The manufacturer's specifications on the contributing components of the noise and error levels are not always explicitly stated. However, the ENOB data for the Tektronix DPO7254 are available[§] and show that, for this 8 bit unit, the effective resolution can

be as low as 5.6 bits for a 2.5 GHz signal or 6.2 bits for a 10 MHz signal (both at 2.5 GHz bandwidth and 50 mV/div vertical settings, with 450 mV input sine wave and 20,000 samples record length). For the 12 bit LeCroy HRO 66Zi, information obtained from the manufacturer[¶] shows that the effective resolution can be as low as 5.0 bits at 2 mV/div setting or 8.7 bits at 1 V/div setting (both for a 1 MHz signal with 2 GS/s sampling rate and 1 million samples record length) or vary between 8.7 bits and 7.4 bits at a 50 mV/div setting for a signal frequency in the range of 20–490 MHz.

The oscilloscope ENOB resulted in a severe limitation on our capability to resolve the full dynamic range of the current signal at high data rates. We found that, when we had set the oscilloscope vertical scale to a range that will capture the high-amplitude current spikes, the low-amplitude part of the signal was below the noise floor of the oscilloscope, preventing accurate power measurement.

2. Limitations of the Differential Probe

Another issue that we encountered was the voltage limitation of the requisite differential probe. The LeCroy AP034 probe used is limited to $+/-0.4$ V maximum differential voltage. There are optional attenuators available with ratios of 10:1 and 20:1, which can bring up the maximum voltage to 4 and 8 V, respectively, but they allow the effective SNR to decrease, which increases measurement uncertainty, reducing the accuracy of the power measurement. This limitation restricts the range of the high voltage that can be applied to the actuator. It also requires the values of the shunt resistor and monitor capacitor to be continually optimized to fit within the probe restriction without yielding a signal so low that it is masked by the oscilloscope noise floor.

3. Signal Multiplexing Approach Attempted

To overcome the oscilloscope SNR, ENOB, and probe limitations, we tried an alternative approach of optimizing the vertical acquisition accuracy of the current signal by selective range multiplexing. Only a brief review of this approach is given here. The current signal was acquired simultaneously on two oscilloscope channels. One channel's vertical scale was set to capture the full amplitude of the spikes. The second channel's vertical scale was set more sensitively to capture the low-amplitude portion of the waveform more accurately while intentionally clipping the high-amplitude portion. A single, hybrid waveform was then reconstructed later in

[§]Tektronix Inc., "DPO70000B/C Series Oscilloscopes, Specifications and Performance Verification Technical Reference," Technical Reference No. 077-0063-05. Data available online at http://www.tek.com/oscilloscope/dpo70000-mso70000-manual-0 [retrieved February 2017].

[¶]LeCroy Inc. Technical Support, private communication, December 2011.

a) Applied Voltage

b) Current (shunt resistor method)

c) Current – Vertical Enlargement

d) Instantaneous power

e) Instantaneous power - vertical enlargement
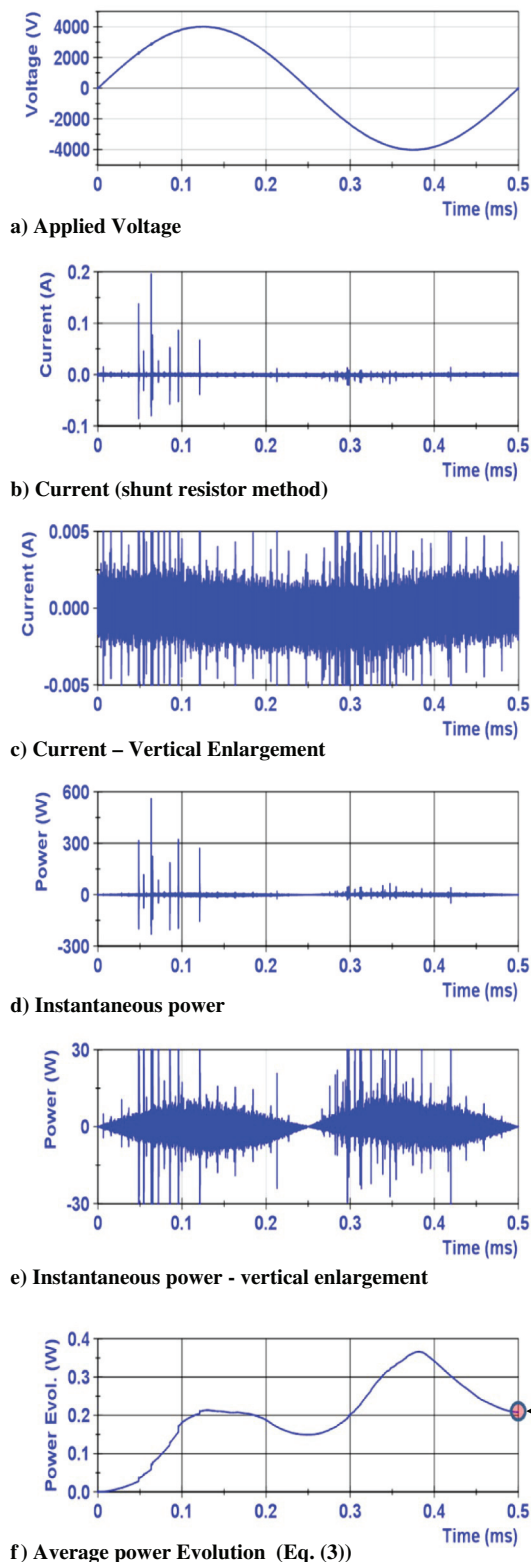

f) Average power Evolution (Eq. (3))

Fig. 11   Typical measurements (shunt resistor method): a) applied voltage, b) current, c) current (vertical enlargement), d) instantaneous power, e) instantaneous power (vertical enlargement), and f) average power evolution.

Fig. 12   Monitor capacitor method: a) Lissajous curve, b) capacitor charge signal, and c) average power evolution.

postprocessing from the valid portions of the two waveforms to create a vertical accuracy-optimized result. It also required careful deskewing of the two scope channels (horizontal calibration to ensure synchronized timing).

This method was tried with the Tektronix DPO7254. However, it was only partially successful. One reason is that, when a signal amplitude is clipped, saturation or overload of the internal amplifier occurs within the oscilloscope. This leads to an undesired overload recovery period that causes the oscilloscope's acquired signal to exhibit unfaithful data during that time. This overload recovery time, as well as the distortion on the unclipped channel in the multiplex threshold region due to the ENOB limit, contributed to our results being more inaccurate than deemed appropriate. We have temporarily abandoned optimizing that approach in favor of another alternative. We did not have the opportunity to try the method with the LeCroy oscilloscope. However, we did observe that, at low levels of clipping, the LeCroy did not exhibit overload recovery flaws observed on the Tektronix.

4. Parasitic Capacitance and Inductance

Another complication is that the effects of combined parasitic L-C circuits in all nonideal components and interconnections become significant at the high frequencies introduced by the spikes. Even though the applied ac voltage waveforms are in the kilohertz frequency range, the current spike frequency content range is from tens to hundreds of megahertz. The parasitic L-C circuits consequently "ring" or oscillate in response to each spike. To be able to allow the parasitic ringing to settle over time without influencing the cumulative power integral, extra vertical range must be provided to prevent clipping of the parasitic ringing. This further restricts the vertical range and accuracy for the relevant signal. Minimizing parasitic properties can significantly improve vertical accuracy and certainty, thus improving power measurement.

F. Nonlinear Signal Compression

An innovative idea was implemented to use a nonlinear, pseudologarithmic compression of the shunt resistor current signal before data acquisition in the oscilloscope. The nonlinear
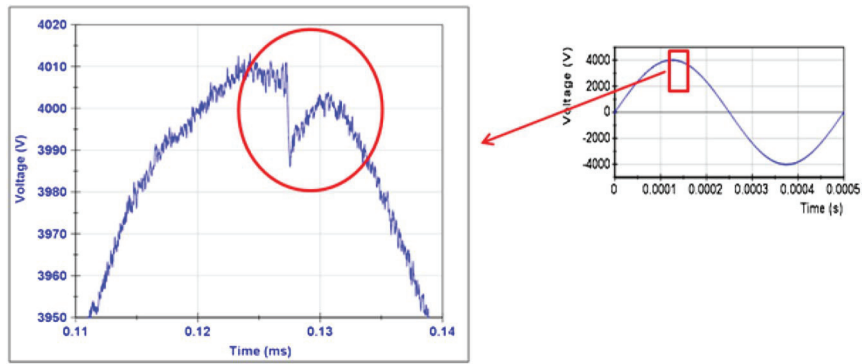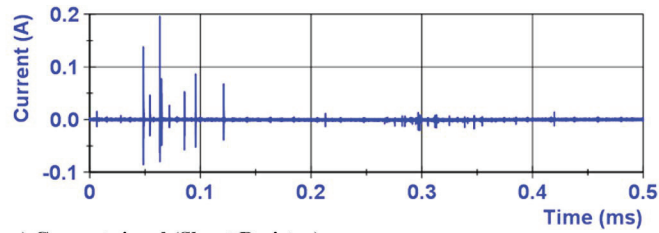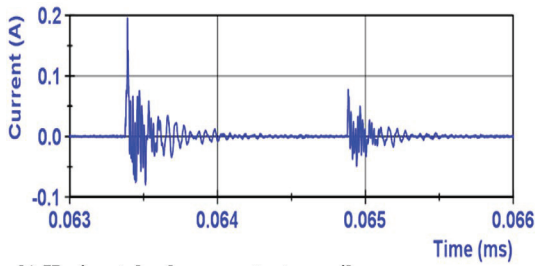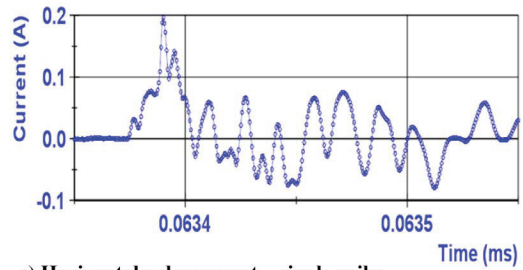
Fig. 13   Applied voltage: detail.

a) Current signal (Shunt Resistor)

b) Horizontal enlargement – two spikes

c) Horizontal enlargement – single spike

Fig. 14   Shunt resistor method: a) current signal, b) horizontal enlargement of two spikes, and c) further enlargement of single spike shown in Fig. 14b. Circles denote measurement samples.
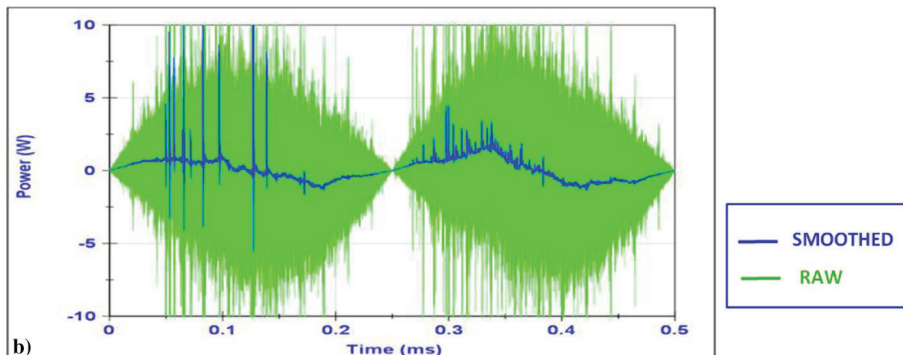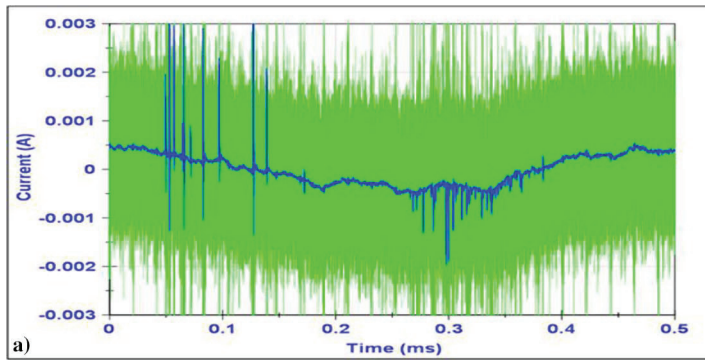

SMOOTHED
RAW

Fig. 15   Visual noise reduction with smoothing: a) current, and b) instantaneous power.
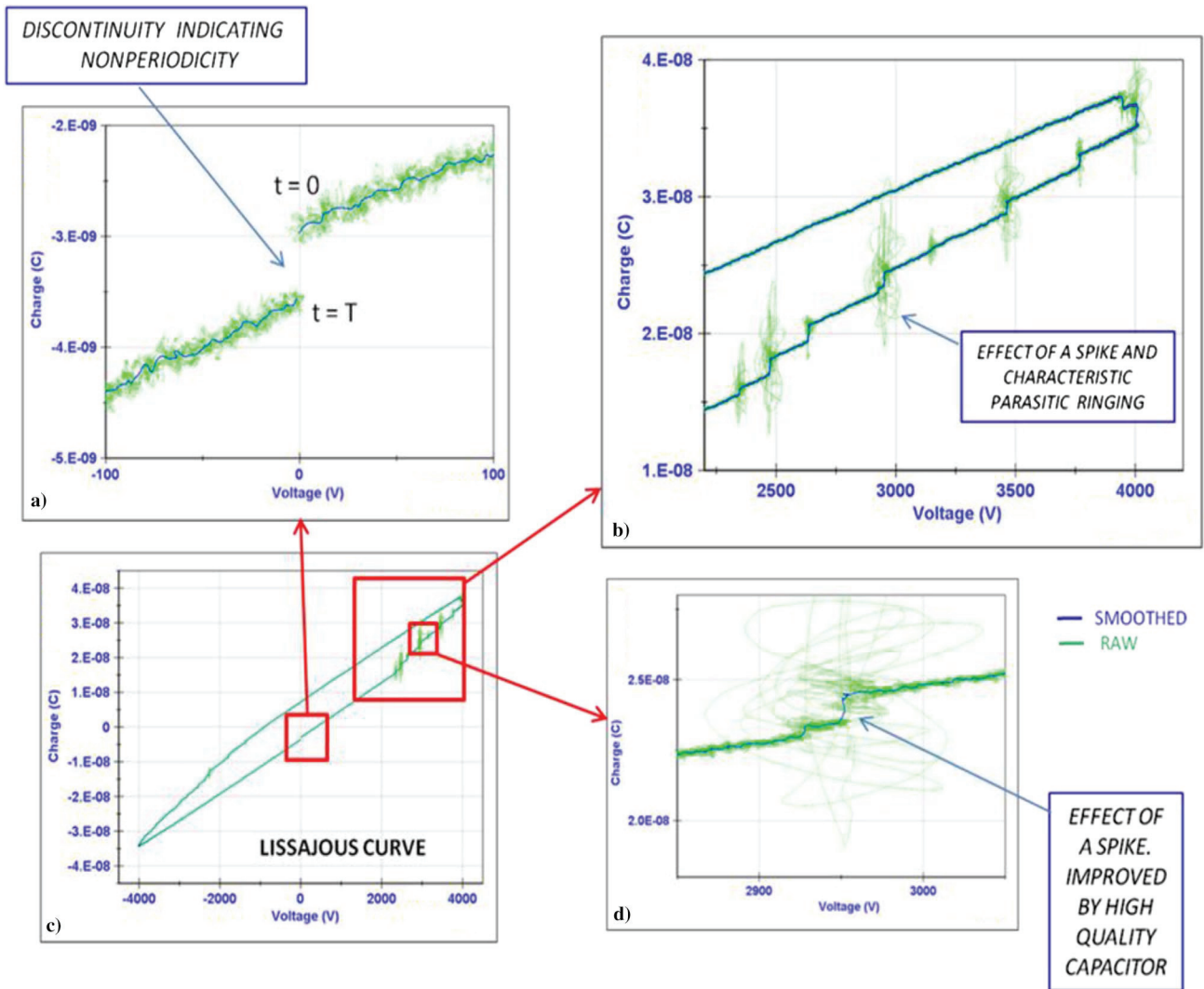
8

Fig. 16 Lissajous curve (detail): a) enlargement of cycle-end discontinuity, b) enlargement of the backward stroke region, c) full-scale curve, and d) enlargement of an individual spike trajectory (green: raw data, blue: smoothed data).

compression reduces the amplitude of the large current spikes without affecting the low-amplitude part of the signal. This allowed setting the oscilloscope vertical scale to a higher sensitivity (fewer volts per division), which lifted the low-amplitude part of the current signal above the fixed noise floor of the oscilloscope, increased its SNR and accuracy, and enabled measurement of the shunt resistor voltage with enough certainty to calculate actuator power. See patent by Laun [23].

An inverse transfer function of the pseudologarithmic compression can be applied in postprocessing to restore the original signal (decompression). However, we initially selected the compression threshold to be active only at the upper range of the high amplitudes, which is statistically infrequent. At the time of publication, we have not yet attempted full signal restoration by decompression. We have used the compressed signal for the calculation, effectively reducing the contribution to the power by the top part of the peaks. The amount of energy lost was limited to a proportionately low level. However, as shown in Sec. III, even without full decompression, the improvement in the low-amplitude capacitive current accuracy outweighed the small loss of energy in the high-amplitude peaks and provided much better overall power accuracy. Full signal decompression will be required when the compression threshold is adjusted to a lower level.

The implementation of the logarithmic compression was done by constructing a simple, passive electrical circuit that consisted of two diodes (Fairchild 1N916) and resistors. An image, a schematic of the circuit, and a plot of the circuit transfer function are shown in Fig. 10.

It is a simple passive circuit that interfaces with a second LeCroy differential oscilloscope probe (the first one is used with the monitor capacitor). The method worked adequately, and as will be shown in the following section, the spike compression idea was successfully demonstrated for a particular set of conditions. Extending the method for a broad range of actuators and parameters requires overcoming several limitations on the use of this approach. Further improvements using more complex passive circuits with improved accuracy as well as active circuit designs are in progress.

III. Results

The results are shown for the test article described previously. The applied ac voltage V was 8 kV p-p at a frequency of 2 kHz (period $T = 0.5$ ms) provided by a Trek Model 20/20 C. The shunt resistor used was 10 Ω, and the monitor capacitor was 230 nF. The data were acquired with the LeCroy HRO 66Zi oscilloscope at the maximum data rate of 2 GS/s. Sixty-four continuous ac cycles were acquired, which filled the available oscilloscope memory. A differential probe (LeCroy AP034) was used to measure the voltage across the monitor capacitor. The shunt resistor voltage was acquired simultaneously on a second channel with and without the compression circuit. The applied actuator voltage was measured with the Trek monitor output on a third channel of the oscilloscope. The acquired data were stored in the oscilloscope and transferred to a desktop computer. National Instruments Diadem software was used to process the results and perform the analysis.
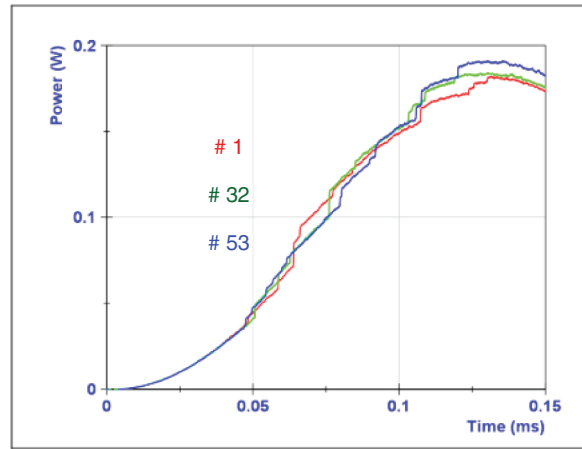
9
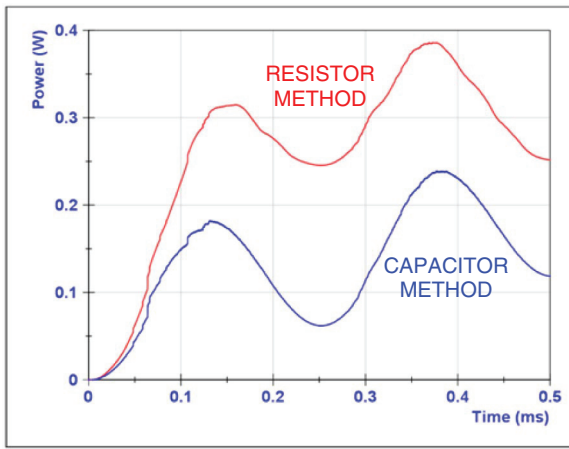
a) Cycle No. 1. – Resistor & Capacitor methods
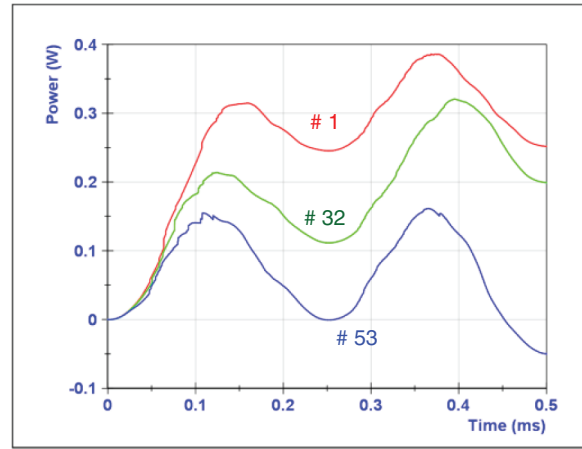
b) Resistor Method - Cycles No. 1, 32, 53
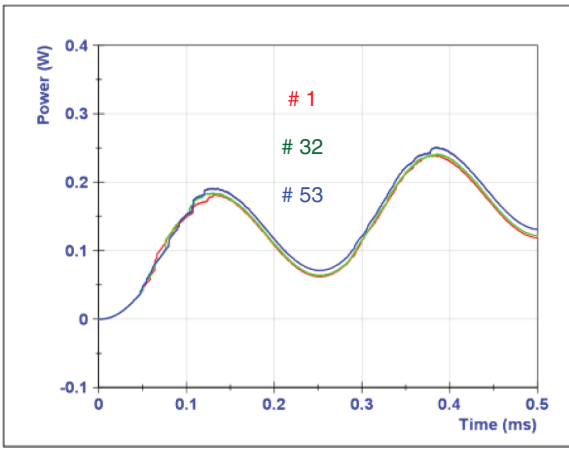
c) Capacitor Method - Cycles No. 1, 32, 53

d) Horizontal enlargement of Fig. 17c

Fig. 17 Power evolution for selected single cycles out of 64 consecutive cycles obtained with resistor and capacitor methods (red: cycle 1; blue: cycle 32; green: cycle 53).

Results are shown first without the nonlinear compression circuit. Figure 11 shows typical results of a single cycle selected from the 64 cycles acquired.

Figure 11a shows the applied sinusoidal voltage. Figure 11b shows the current calculated from the shunt resistor voltage. We observe spikes but no observable low-amplitude signal. The spikes are large, and the low-amplitude current cannot be discerned without significant vertical magnification. Figure 11c shows the required vertical magnification with clipped spikes. It is evident that the spikes are superposed on a low-amplitude, very noisy signal. The crest factor of the signal is quite large (ratio of the large-amplitude spikes to the low-amplitude part of signal). Figure 11d shows the instantaneous power calculated by multiplying the voltage and the current, sample by sample [Eq. (1)]. Figure 11e shows a vertical magnification of the instantaneous power, showing the region corresponding to the low-amplitude part. Figure 11f shows the cumulative average power evolution obtained by integration of the instantaneous power and period normalization [Eq. (3)]. The last point at $t = T$ is the average power for the cycle [Eq. (4)].

Figure 12 shows results from the monitor capacitor method for the same cycle. Figure 12a shows the Lissajous curve. The area enclosed by the curve normalized by the period is equal to the power of the cycle [Eq. (8)]. Figure 12b shows the charge signal [capacitor voltage times the capacitance, Eq. (5)]. Steps are observed on the curve that corresponds to charge deposited by the current spikes. Figure 12c shows the averaged power evolution.

Note that displaying these signals on a computer display or a printer can be misleading because much of the details are masked by their limited pixel resolution. Enlargements of sections of

the signal are required. Detailed looks into these curves are to follow.

A. Detailed Look into the Voltage and Current Signals

Figure 13 provides a detailed look of the voltage signal. A portion of the signal is magnified. The signal shown has been smoothed slightly to eliminate higher-frequency noise for visual inspection. A sharp dip in the signal, followed by a recovery to the original waveform, is observed. This dip is triggered by a typical current spike, which is caused by an actuator microdischarge occurring at the leading edge of the dip. The power supply cannot keep the prescribed applied voltage when the microdischarge current spike suddenly loads the output. The power supply recovery time is quite fast. The dip in the voltage is small, about 20 V out of 8 kV p-p, and is relatively minor. For practical purposes, it can be assumed that the applied voltage is a smooth function, and these dips can be ignored as long as the power supply system has adequate response to these quick load changes. If the power supply system does not have adequate performance, the input voltage signal will be affected significantly.

Figure 14 is a detailed look at the current signal. Figure 14a repeats the raw signal. Figure 14b is a horizontal-only magnification of two close spikes, and Fig. 14c is further horizontal magnification of one of them that reveals more spike details. It shows that a spike consists of an initial pulse followed by multiple resonant oscillations superimposed over each other. The initial current impulse is from a single microdischarge or streamer and likely to be the charge transfer of the actuator itself. The oscillations, or "ringing", are caused by various resonant circuits composed of parasitic inductances and capacitances in the connecting circuit reacting to the first pulse.

10
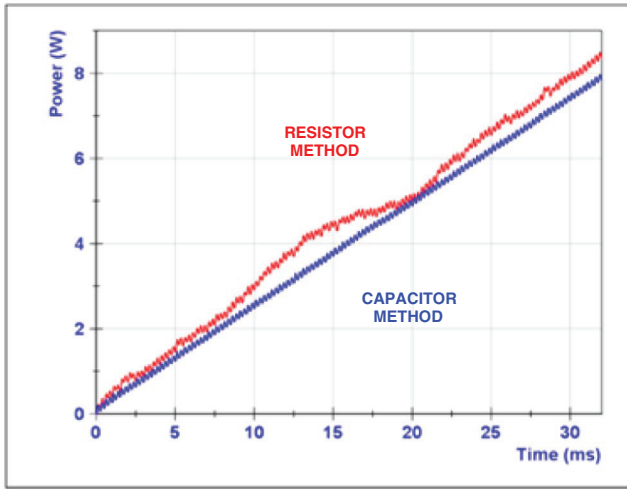
a) Original circuit
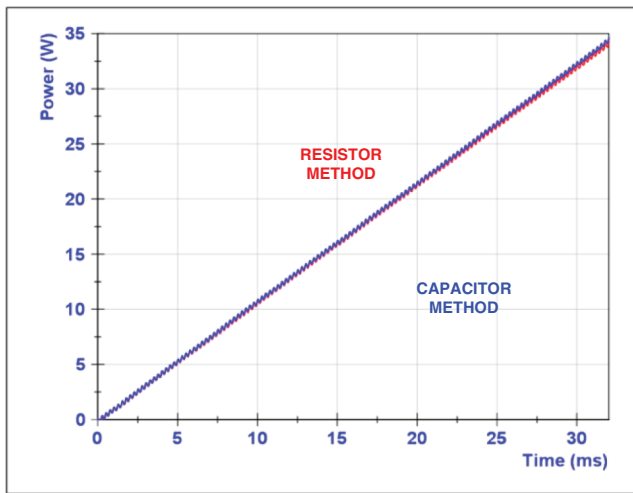
b) With compression circuit

Fig. 18   Comparison of cumulative power evolution for 64 consecutive cycles: a) original shunt resistor circuit, and b) circuit with diode-based nonlinear signal compression.

The points on the curve marked by circles in Fig. 14c are the acquired data points. It is evident that the data rate is more than sufficient to resolve the spikes.

Figure 15 is a vertical enlargement of the low-amplitude portion of the actuator signals. Figure 15a shows the current, and Fig. 15b shows the instantaneous power. The green curves are the raw signals. The blue curves are the raw signals smoothed with a running average moving window. The width of the window for these plots was selected for optimal visual inspection; the calculations were made

with the original raw signal. The smoothing helps distinguish the underlying signal from the instantaneous high-frequency noise that visually masks the plots. It shows that the low-amplitude current consists of a nonsinusoidal waveform. The expected waveform frequency of the applied voltage can be identified. This low-amplitude current consists of the cold capacitive actuator displacement current within the actuator and additional currents caused by other sources associated with the plasma processes, such as variable surface charge movements, volume charge equalizations, corona discharge currents occurring between spikes, and other unidentified current sources.

B.   Detailed Look into the Lissajous Curve

The Lissajous curve is shown in Fig. 16. Enlargements of several sections as marked on Fig. 16c are included. The plots reveal features that were not observed before. Figure 16b shows an enlargement of the section that corresponds to backward stroke region. Figure 16d is a further enlargement of one feature. The spiky behavior as exhibited in Fig. 3b is much reduced, and the curve is smoother. It is apparent that features that appeared to look like spikes with ringing in prior published work, for example as shown in Fig. 3b, are in fact steps on the curve accompanied by nearby trajectories. The trajectories are caused by ringing on the charge and voltage signals attributed primarily to parasitic impedances.

The green curve in the plots is the raw signal. The blue curve is a smoothed copy of the green (raw) signal used for the integration of the curve to calculate the area. It is clear that the steps on the curve are attributed to spikes in the actuator current and correspond to the steps observed in the charge signal in Fig. 12b. Each spike deposits charge on the monitor capacitor that increases its instantaneous charge at a relatively constant applied actuator voltage. The forward stroke part of the signal exhibits much smaller steps.

The steps in the Lissajous curve have a profound effect on the results of the area integration. The area would be different if the steps were smoothed out and profoundly different if the steps did not exist. In the latter case, the Lissajous curve would continue smoothly around and have a much narrower, elliptical shape, hence a different area and therefore different power consumption result.

Another interesting feature, which was not observed before in published literature, is the discontinuity in the curve between the point that corresponds to $t = 0$ and the point corresponding to, $t = T$ as shown in the enlargement in Fig. 16a. A repetitive waveform would not have a discontinuity there and would just be observed as an uninterrupted line. Therefore, the Lissajous curve is not a closed curve as expected. Examination of the derivation of Eq. (8) shows that the integration that provides the power calculation over a period T is still valid also for an open curve. Two reasons for the gap in the curve are asymmetric residual surface charges and the nonperiodicity of the signal due to the random distribution and energy of the current spikes from discharges. Each cycle in the sequence of the consecutive 64 cycles acquired is not periodic and is characterized by different initial conditions. Surface charges in DBD actuators were addressed by Opaits et al. [24] for the case of nanosecond pulsing operation
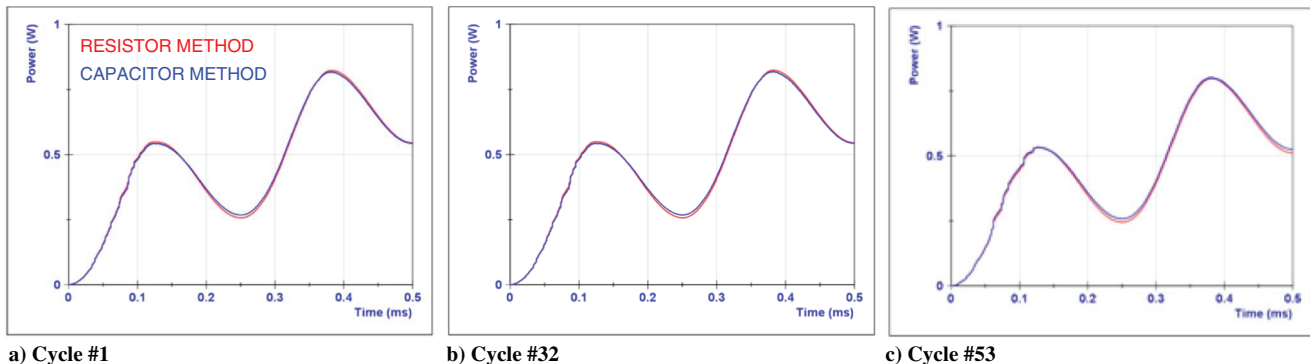

a) Cycle #1

b) Cycle #32

c) Cycle #53

Fig. 19   Effect of compression circuit. Power evolution for three selected cycles out of 64 consecutive cycles: a) cycle 1, b) cycle 32, and c) cycle 53 (red: shunt resistor method; blue: monitor capacitor method).
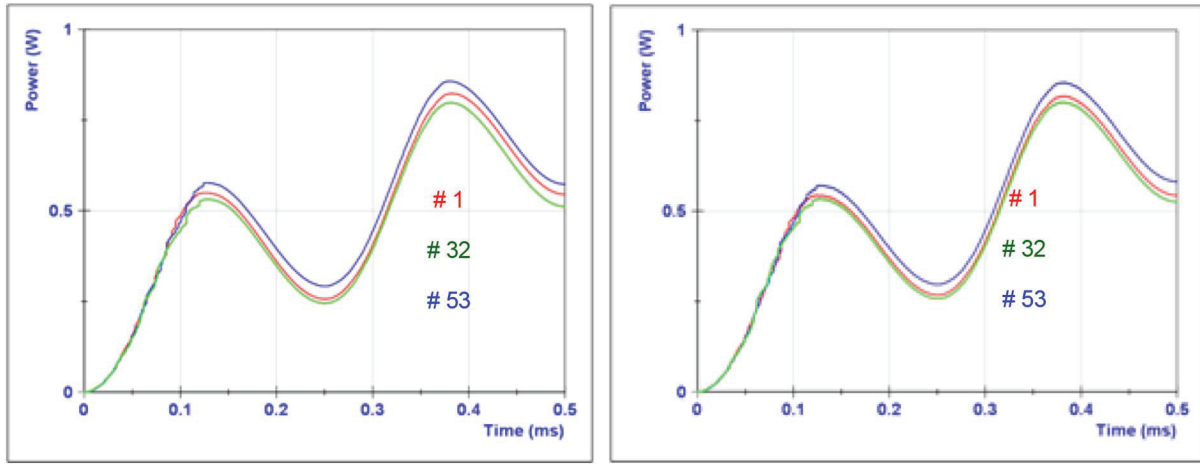
11

a) Resistor method with Compression   **b) Capacitor method**

Fig. 20 **Power evolution for three selected cycles out of 64 consecutive cycles (red: cycle 1; green: cycle 32; blue: cycle 53): a) shunt resistor method with compression, and b) monitor capacitor method.**
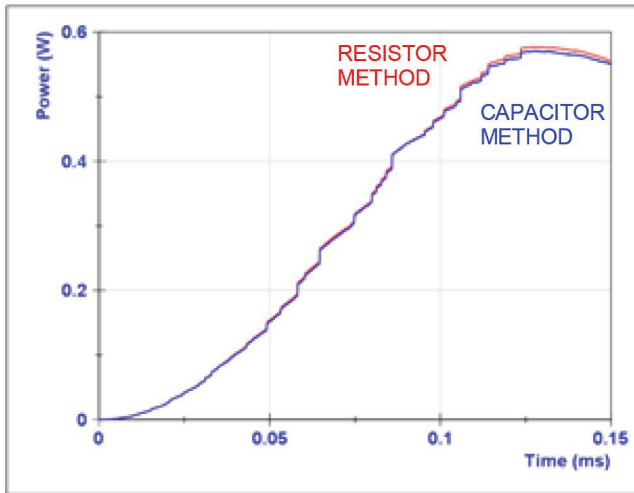

Fig. 21 **Enlargement of Fig. 19b, power evolution, cycle 32 (red: shunt resistor method with compression; blue: monitor capacitor method).**

(NS-DBD), and by Enloe et al. [25] for the conventional AC-DBD actuators. All measurements in our experiment were recorded after the initial power-on transient subsided.

C.   Power Calculations Without Compression Circuit

The actuator power evolution was calculated for the 64 consecutive cycles (acquired without the advantage of the diode compressor circuit). Calculations are first shown for selected single cycles. Figure 17a shows a comparison of the average power evolution using the simultaneous shunt resistor and monitor capacitor methods for cycle number 1. The cycle-averaged power is the reading at $t = T = 0.5$ ms. As can be seen for this cycle only, the resistor method power is approximately 80% higher than the capacitor method.

Figure 17b shows a comparison of power consumed in three separate cycles in the series calculated using the resistor method (cycle numbers 1, 32, and 53). The plots were shifted vertically to all start at zero power for comparison purposes. There are large single-cycle discrepancies including one cycle (number 53) with an irrational negative power result. The poor SNR at the oscilloscope settings (excessive noise floor) is the primary contributor to the variability of the results.

Figure 17c compares the power of the same three cycles using the capacitor method data instead. Again, the plots were shifted vertically to all start at zero power for comparison purposes. They match within

10%. This superior performance is primarily due to the limited dynamic range and adequate voltage level of the monitor capacitor signal, which allows the effect of the scope noise floor to be diminished and consequently improves the SNR enough for accurate power calculation.

Figure 17d shows an enlargement of the first quarter $(0 \leq t \leq 0.15$ ms) of Fig. 17c to reveal the nonrepetitive nature of the instantaneous actuator power. The steps on the curve in the region of the backward stroke are noticeable. They correspond to the power contributed by individual microdischarges; each microdischarge adds a discrete amount to the cumulative power. There are smaller steps in the forward stroke region $(t \geq 0.35$ ms). The random occurrence and intensity of the spikes contribute to random deviation of the curve from its trajectory and hence leads to the variability of the results.

Figure 18a shows the cumulative average power evolution over the full 64 cycles for the resistor method and the capacitor method. For both methods, the integration was performed continuously from $t = 0$ to 32 ms. If each of the 64 cycles is truly periodic, then the plots should lie along a straight line that indicates a constant average power consumption.

As can be seen in the figure, even though the capacitor method appears to follow the expected straight line, the resistor method does not. A different set of 64 consecutive samples generated a different curve that similarly deviated from the straight line. The conclusion is that the resistor method calculations without the advantage of the nonlinear compression are inaccurate. The reason is that the contribution of the low-amplitude portion of the instantaneous power signal to the integration causes the result to diverge from the track of actual power consumption. The low-amplitude portion of the waveform represents nearly 99% of the cycle time and, ultimately, a sizeable portion of the total cycle power. The low-amplitude portion is inaccurate in this case because of the poor oscilloscope SNR resulting from a high dynamic range signal. The low-amplitude signal was below the noise floor and ENOB threshold of the oscilloscope. Even though the high-amplitude current spikes are accurately acquired at this setting, their contribution to the integration result apparently is not enough to overwhelm the effects of the inaccuracy of the low-amplitude portion of the waveform.

As a note regarding the resistor method, the noise and dc bias inherent to the oscilloscope generated a complex baseline that needed to be accounted for to prevent large cumulative power errors. Because of the low SNR and high uncertainty within the oscilloscope at these settings, it was impossible to obtain an accurate dc bias to calibrate the oscilloscope data. Therefore, for analysis purposes, the dc component of the entire 64-cycle current signal was calculated and subtracted. Not doing so would have caused excessive divergence of the cumulative power calculations and prevented local comparison of the resistor method to the capacitor method.

a) Power level variation

b) Power level variation with compression

c) Power level distribution

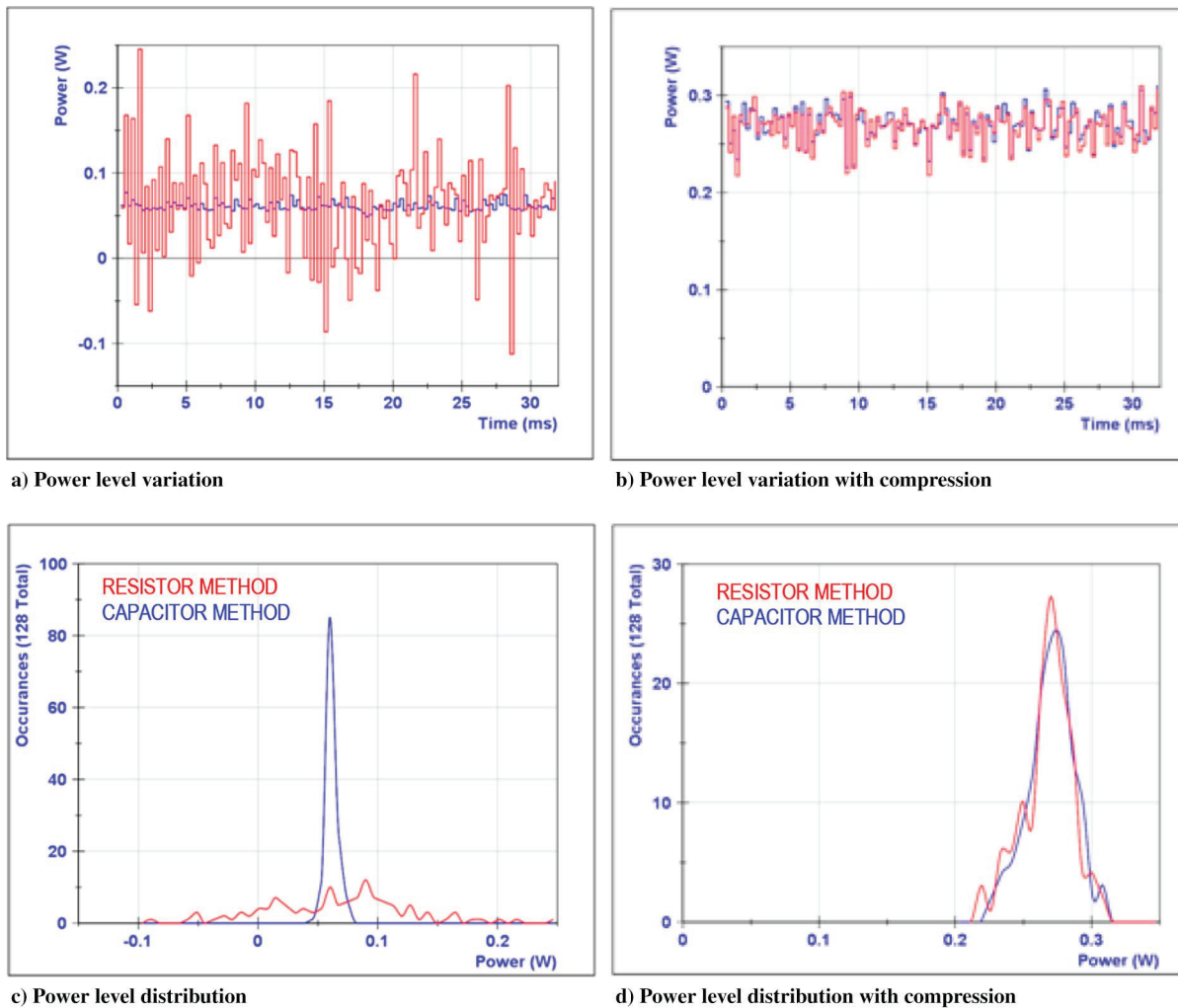d) Power level distribution with compression

Fig. 22 Distribution of averaged power for 64 consecutive cycles, calculated at half-cycle increments, without compression (8 kVp-p), and with compression (12 kVp-p). Red: shunt resistor method. Blue: monitor capacitor method.

D. Power Measurements with Nonlinear Signal Compression Circuit

In an attempt to remedy the apparent inaccuracy of the shunt resistor method, we have implemented the logarithmic signal compression circuit described previously. The goal is to compress the amplitude of the current spikes, to reduce the dynamic range of the signal, and to elevate the low-amplitude portion above the oscilloscope noise floor and ENOB limitations. Similar to the previous case, 64 cycles were acquired with the same actuator, but with an applied voltage of 12 kV p-p instead of 8 kV p-p. The different value of applied voltage was required because the new compressor monitor circuit impedance influenced the behavior of the actuator at low to moderate power levels. The impedance increase in the monitor circuit was required to increase the voltage across the shunt enough to activate the compressing effect of the passive diodes.

The results are shown in Fig. 18b. As can be seen, both methods follow a straight line, which indicates that the resistor method performed very well using this approach. The improvement is attributed to the increased SNR and accuracy facilitated by the compression of the signal. This was accomplished by increasing the vertical sensitivity setting of the oscilloscope to a smaller value of V/div, which allowed us to obtain a more accurate reading of the small-amplitude part of the current signal, which was now raised above the noise floor of the oscilloscope. The calculation of the resistor method power was mostly free of contamination of random noise from the scope. It clearly demonstrates that the presence of random instrument noise greatly affects the results of the integration used to calculate the power when using the resistor method.

Figure 19 shows comparisons between the resistor and capacitor methods, for three selected cycles (numbers 1, 32, and 53). The agreement is excellent (contrast with Fig. 17a).

Now that the two methods converge, attention can be paid to the variability between the different cycles:

Figure 20 shows a comparison of three selected cycles for each method. The variability of the single-cycle actuator power over a limited time period is approximately 10%.

Figure 21 shows an enlargement of the comparison of the resistor method and capacitor method power evolution signals. The steps in the curves follow each other closely, increasing the confidence in the accuracy of the results using the compression approach. This validates that the mild compression of only the highest current spike amplitudes without applying postprocessing decompression (as discussed in Sec. II.F) does not contribute significant error in this case. Improvements are being made for future compressor designs and postprocessing that will further improve the accuracy and matching between the two methods for a large population of test article geometries and range of parameters.

For increased temporal resolution and statistical analysis, Fig. 22 shows comparisons of averaged power for half-cycles of the same data. The 128 half-cycle power values are calculated with both the resistor and the capacitor methods. Figure 22a is a bar chart showing the variation of the half-cycle power values without compression and poor SNR (with 8 kV p-p applied voltage). A bar chart of the data with the compression circuit installed (with 12 kV p-p applied voltage) is shown in Fig. 22b. These results are cast in the form of histograms in Figs. 22c and 22d.

The figures show that there is a large discrepancy between the two methods when compression was not used (Fig. 22c). The standard deviation of the capacitor method is narrow as expected and appears representative. However, the standard deviation of the resistor method is extremely large deeming the results unreliable.

When the diode compression circuit is used and the oscilloscope SNR is consequently increased, the two methods converge to practically the same average power and standard deviation, as shown in Fig. 22d.

IV. Discussion

We have shown that the nature of the current signal, which is composed of large spikes superimposed on a low-amplitude current, forces the data acquisition instrument to become the unavoidable source of inaccuracies in current-based DBD actuator power measurements. The issue could be resolved by using data acquisition equipment with higher bit resolution (e.g., 16 bit or higher) matched with higher-quality analog hardware that can perform with adequate SNR. However, we are not aware of standard laboratory class hardware that has the high bit resolution in combination with the required high analog frequency bandwidth, high sample rate, and sufficiently low analog noise. Therefore, we have used available high-speed oscilloscopes as data acquisition systems. It was disappointing to find that, even with a 12 bit high-speed oscilloscope, which is not common in the market, we still had limitations on the capability to perform accurate power measurements with the shunt resistor method.

Choosing to perform time-accurate comparisons rather than statistical comparisons between the shunt resistor and monitor capacitor methods required simultaneous measurements, which increased the technical complexity of the project. However, it had the advantage of controlling the experimental parameters. It is difficult to reproduce the same operating conditions with one setup for the resistor method and a separate setup for the capacitor method. One issue is that the performance and the physics associated with the discharge behavior appears to be coupled to the properties of the power supply system and to the monitor circuit components and interconnects. In addition, the actuator does not repeat the same waveform twice, which makes comparing single cycles of different methods at different times nearly impossible. In addition, there is actuator heating, ozone production, NO_x production, and ambient air temperature and humidity that influence the operational conditions. Therefore, separate experiments may not be identical even with same applied voltage level, frequency, and waveform. Therefore, the added complexity of our approach was justified.

V. Conclusions

This paper reports on the progress made toward accurate dielectric barrier discharge (DBD) actuator power measurement and is not a final conclusion. It is hoped that the reported experience, techniques, and observations will be useful to the DBD plasma actuator research community, especially to those who come from a fluid mechanics background and may not be aware of several technical challenges involved with measuring plasma processes. The immediate conclusion is that the capacitor method is consistently more reliable, intrinsically more accurate, and simpler to implement with common equipment. Careful selection of a quality monitor capacitor is important, though. Another conclusion is that careful attention has to be paid to the physical limitations of the instrumentation, which may not be self-evident.

Future plans are to continue this work. The first goal will be to extend the techniques to a broad range of parameters and enable the study of different actuator geometries and designs under a broad range of operating conditions. The present experiments and conclusions are based on a single actuator design with limited conditions, and substantiation of conclusions is needed. It is planned to pursue the signal compression approach and develop it further so that it can be used under a broad range of operating conditions.

The present experiments were performed with relatively high-end equipment, and it is planned to study the error bounds on the results when more common laboratory equipment is used. It is understood that it is not feasible to routinely perform massive data acquisition and processing as described in this paper. The ultimate goal is to produce a simplified and accurate actuator power measurement technique with known error bounds.

References

[1] Moreau, E., "Airflow Control by Non-Thermal Plasma Actuators," *Journal of Physics D: Applied Physics*, Vol. 40, No. 3, 2007, pp. 605–636.
doi:10.1088/0022-3727/40/3/S01

[2] Corke, T. C., Post, M. L., and Orlov, D. M., "SDBD Plasma Enhanced Aerodynamics: Concepts, Optimization and Applications," *Progress in Aerospace Sciences*, Vol. 43, Nos. 7–8, 2007, pp. 193–217.
doi:10.1016/j.paerosci.2007.06.001

[3] Corke, T. C., Post, M. L., and Orlov, D. M., "Single Dielectric Barrier Discharge Plasma Enhanced Aerodynamics: Physics, Modeling and Applications," *Experiments in Fluids*, Vol. 46, No. 1, 2009, pp. 1–26.
doi:10.1007/s00348-008-0582-5

[4] Corke, T. C., Enloe, C. L., and Wilkinson, S. P., "Dielectric Barrier Discharge Plasma Actuators for Flow Control," *Annual Reviews of Fluid Mechanics*, Vol. 42, 2010, pp. 505–529.
doi:10.1146/annurev-fluid-121108-145550

[5] Benard, N., and Moreau, E., "Electrical and Mechanical Characteristics of Surface AC Dielectric Barrier Discharge Plasma Actuators Applied to Airflow Control," *Experiments in Fluids*, Vol. 55, No. 11, 2014, Paper 1846.
doi:10.1007/s00348-014-1846-x

[6] Kotsonis, M., "Diagnostics for Characterisation of Plasma Actuators," *Measurement Science and Technology*, Vol. 26, No. 9, 2015, Paper 092001.
doi:10.1088/0957-0233/26/9/092001

[7] Roupassov, D. V., Nikipelov, A. A., Nudnova, M. M., and Starikovskii, A. Y., "Flow Separation Control by Plasma Actuator with Nanosecond Pulse Periodic Discharge," AIAA Paper 2008-1367, 2008.

[8] Starikovskiy, A., Gordon, S., Post, M., and Miles, R., "Barrier Discharge Development and Thrust Generation at Low and High Pressure Conditions," AIAA Paper 2014-0329, Jan. 2014.

[9] Thomas, F. O., Corke, T. C., Iqbal, M., Kozlov, A., and Schatzman, D., "Optimization of Dielectric Barrier Discharge Plasma Actuators for Active Aerodynamic Flow Control," *AIAA Journal*, Vol. 47, No. 9, Sept. 2009, pp. 2169–2178.
doi:10.2514/1.41588

[10] Kriegseis, J., Möller, B., Grundmann, S., and Tropea, C., "Light Emission, Discharge Capacitance and Thrust Production of DBD Plasma Actuators," AIAA Paper 2011-155, Jan. 2011.

[11] Kriegseis, J., Schröter, D., Grundmann, S., and Tropea, C., "Online-Characterization of Dielectric Barrier Discharge Plasma Actuators for Optimized Efficiency of Aerodynamical Flow Control Applications," *Journal of Physics: Conference Series*, Vol. 301, June 2011, Paper 012020.
doi:10.1088/1742-6596/301/1/012020

[12] Kriegseis, J., Möller, B., Grundmann, S., and Tropea, C., "Capacitance and Power Consumption Quantification of Dielectric Barrier Discharge (DBD) Plasma Actuators," *Journal of Electrostatics*, Vol. 69, No. 4, Aug. 2011, pp. 302–312.
doi:10.1016/j.elstat.2011.04.007

[13] Manley, T. C., "The Electric Characteristics of the Ozonator Discharge," *Journal of the Electrochemical Society*, Vol. 84, No. 1, 1943, pp. 83–96.
doi:10.1149/1.3071556

[14] Wagner, H.-E., Brandenburg, R., Kozlov, K. V., Sonnenfeld, A., Michel, P., and Behnke, J. F., "The Barrier Discharge: Basic Properties and Applications to Surface Treatment," *Vacuum*, Vol. 71, No. 3, 2003, pp. 417–436.
doi:10.1016/S0042-207X(02)00765-0

[15] Borcia, G., Anderson, C. A., and Brown, N. M. D., "Dielectric Barrier Discharge for Surface Treatment: Application to Selected Polymers in Film and Fibre Form," *Plasma Sources Science and Technology*, Vol. 12, No. 3, 2003, pp. 335–344.
doi:10.1088/0963-0252/12/3/306

[16] Pons, J., Moreau, E., and Touchard, G., "Asymmetric Surface Dielectric Barrier Discharge in Air at Atmospheric Pressure: Electrical Properties and Induced Airflow Characteristics," *Journal of Physics D*, Vol. 38, No. 19, pp. 3635–3642, Sept. 2005, doi:10.1088/0022-3727/38/19/012

[17] Hoskinson, A. R., "Measurements and Simulations of Surface Dielectric Barrier Discharges Used as Plasma Actuators," Ph.D. Dissertation, Univ. of Wisconsin, Madison, WI, June 2009.

[18] Poon, D.-K., "Separation Control Using Plasma Actuators: Experimental Studies of Plasma Actuator Performance," M.S. Thesis, The Univ. of Minnesota, Minneapolis, MN, Jan. 2011.

[19] Grundmann, S., and Tropea, C., "Experimental Damping of Boundary-Layer Oscillations Using Plasma Actuators," *International Journal of Heat and Fluid Flow*, Vol. 30, No. 3, 2009, pp. 394–402. doi:10.1016/j.ijheatfluidflow.2009.03.004

[20] Kriegseis, J., Grundmann, S., and Tropea, C., "Power Consumption, Discharge Capacitance and Light Emission as Measures for Thrust Production of Dielectric Barrier Discharge Plasma Actuators," *Journal of Applied Physics*, Vol. 110, No. 1, 2011, Paper 013305. doi:10.1063/1.3603030

[21] Enloe, C. L., McLaughlin, T. E., VanDyken, R. D., Kachner, K. D., Jumper, E. J., and Corke, T. C., "Mechanisms and Responses of a Single Dielectric Barrier Plasma Actuator: Plasma Morphology," *AIAA Journal*, Vol. 42, No. 3, 2004, pp. 589–594. doi:10.2514/1.2305

[22] Enloe, C. L., McLaughlin, T. E., VanDyken, R. D., Kachner, K. D., Jumper, E. J., Corke, T. C., Post, M., and Haddad, O., "Mechanisms and Responses of a Single Dielectric Barrier Plasma Actuator: Geometric Effects," *AIAA Journal*, Vol. 42, No. 3, 2004, pp. 595–604. doi:10.2514/1.3884

[23] Laun, M. C., "Dynamic Range Enhancement of High-Speed Electrical Signal Data via Non-Linear Compression," U.S. Patent 9,264,154 B1, 16 Feb. 2016.

[24] Opaits, D. F., Neretti, G., Likhanskii, A. V., Zaidi, S., Shneider, M. N., and Miles, R. B., "Experimental Investigation of DBD Plasma Actuators Driven by Repetitive High Voltage Nanosecond Pulses with DC or Low-Frequency Sinusoidal Bias," AIAA Paper 2007-4532, June 2007.

[25] Enloe, C. L., Font, G. I., McLaughlin, T. E., and Orlov, D. M., "Surface Potential and Longitudinal Electric Field Measurements in the Aerodynamic Plasma Actuator," *AIAA Journal*, Vol. 46, No. 11, Nov. 2008, pp. 2730–2740. doi:10.2514/1.33973